Gyrokinetic simulations including the centrifugal force in a rotating tokamak plasma

F. J. Casson,[1] A. G. Peeters,[2] C. Angioni,[3] Y. Camenen,[1] W. A. Hornsby,[1] A. P. Snodin,[1] and G. Szepesi[1]
[1]*Centre for Fusion, Space, and Astrophysics, University of Warwick, CV4 7AL, Coventry, United Kingdom*
[2]*University of Bayreuth, Universitaetsstrasse 30, Bayreuth 95447, Germany*
[3]*Max-Planck-Institut für Plasmaphysik, IPP-EURATOM Association, D-85748 Garching bei München, Germany*

(Received 14 May 2010; accepted 27 August 2010; published online 19 October 2010)

Tokamak experiments operate with a rotating plasma, with toroidal velocity which can be driven externally but can also arise spontaneously. In the frame that corotates with the plasma, the effects of the centrifugal force are felt through a centrifugal drift and an enhanced mirror force [Peeters *et al.*, Phys. Plasmas **16**, 042310 (2009)]. These inertial terms become important in the case of strong rotation, as is common in spherical devices, and are also important for heavy impurity ions even at small toroidal velocities. In this work, the first gyrokinetic simulations including the centrifugal force in a strongly rotating plasma are presented. The enhanced mirror force redistributes density over a flux surface and modifies the trapping condition, destabilizing trapped electron modes. At intermediate scales this can result in promotion of the trapped electron mode over the ion temperature gradient (ITG) mode as the dominant instability, which under marginal conditions could result in an enhanced electron heat flux. The centrifugal drift acts to damp the residual zonal flow of the geoacoustic mode, while its frequency is increased. For nonlinear ITG dominated turbulence, increased trapped electron drive and reduced zonal flow lead to an increase in ion heat diffusivity if the increased rotation is not accompanied by rotational shear stabilization. An increased fraction of slow trapped electrons enhances the convective particle pinch, leading to an increase in the steady state density gradient with strong rotation. Linear ITG mode results show an increased pinch of heavy trace impurities due to their strong centrifugal trapping. © *2010 American Institute of Physics*. [doi:10.1063/1.3491110]

I. INTRODUCTION

Plasma rotation in tokamaks has long been known to play a key role in the formation of transport barriers[1,2] and in the suppression of resistive wall modes.[3] In a large aspect ratio tokamak, the deuterium Mach number is usually observed to be low, and is expected to be low in a future reactor with lower relative momentum input from neutral beams. On this basis, rotational effects were not originally included in the gyrokinetic codes used to model turbulent transport. The observation of spontaneous plasma rotation in the absence of an external momentum source[4,5] has led to a renewed interest in plasma rotation and a focus on rotation measurement. Recent observations of Mach numbers up to 0.7 now challenge the assumption of low Mach number in conventional aspect ratio devices,[6] while spherical tokamaks have long been known to operate at Mach numbers approaching unity.[7,8] Even at low bulk ion rotation, the Mach number for heavy impurities can reach supersonic values, with the result that the distribution and transport of these impurities are strongly influenced by inertial forces. Developing an understanding of impurity transport mechanisms will be of key importance in order for a future fusion reactor to successfully control core impurity buildup.

A number of studies have examined the effect of strong rotation on neoclassical transport,[9–15] but the influence of strong rotation on turbulent transport is largely unaddressed. A series of previous works[16–18] have extended the gyrokinetic formalism to the rotating frame of reference, in which rotational effects appear as inertial forces[18] or modified effective fields.[19] The Coriolis force is known to play an important role in the anomalous momentum transport that leads to spontaneous rotation,[20–22] and its impact on heat and particle transport has also been studied.[23] The effect of the centrifugal force on particle and heat transport has been examined in a fluid model,[23] but until now has not been examined using the full gyrokinetic model.

In the present work, the effects of strong rotation are examined for the first time in the gyrokinetic model, through the inclusion of the centrifugal force. Linear and nonlinear gyrokinetic simulations in toroidal geometry including all the inertial terms are presented. Simulations are performed with the Vlasov flux tube code GKW.[24,25]

This paper is structured as follows: Sec. II presents the gyrokinetic equations solved, highlighting the appearance of new inertial terms. Section III introduces the simulated system, and Sec. IV A discusses the consequences of strong rotation for the ion temperature gradient (ITG) mode and trapped electron mode (TEM) drift wave instabilities. Linear results for particle and impurity transport are presented in Sec. IV B, and the effect on the zonal geoacoustic mode (GAM) is examined in Sec IV C. Early nonlinear results are presented in Sec. V, and conclusions are drawn in Sec. VI.

II. THEORETICAL FRAMEWORK

The gyrokinetic formalism in the rotating frame was originally detailed in Ref. 16 and later developed in Ref. 18. A full description of the GKW code is detailed in Ref. 25 and the code is available from the associated library (and http://gkw.googlecode.com). The centrifugal effects described here have been implemented in the code since the publication of Ref. 25.

In this section, the details of the implementation of the inertial terms in the local model of GKW are presented, and the consequences for particle density and trapping are discussed. For context, relevant parts of Refs. 18 and 25 are reiterated here.

We consider a local flux-tube gyrokinetic model formulated in the comoving frame that rotates with the plasma. The frame rotates rigidly with toroidal angular velocity $\boldsymbol{\Omega}=-\Omega\nabla Z$, while the plasma rotates with angular velocity $\boldsymbol{\omega}_\phi(\psi)=-\omega_\phi(\psi)\nabla Z$, where $\psi=r/R_A$ is the dimensionless radial coordinate. The frame rotation is chosen such that $\Omega=\omega_\phi$ on the flux surface under consideration, with the local plasma toroidal velocity $\boldsymbol{u}_t=R\boldsymbol{\Omega}\times\nabla R$ in the direction of $\boldsymbol{B}_t$. We define also the dimensionless toroidal Mach number $u=R_A\Omega/v_{\mathrm{th}}$ as the rotational toroidal speed of the frame (evaluated at the major radius of the magnetic axis R_A) normalized by the ion thermal velocity $v_{\mathrm{th}}=\sqrt{2T_i/m_i}$ (which may differ from other definitions) on the local flux surface.

Starting from Eqs. 19 and 28 of Ref. 18 the equations of gyrocenter motion in the rotating frame, local model, and low beta limit can be written as

$$m v_\parallel \frac{dv_\parallel}{dt} = -\frac{d\mathbf{X}}{dt}\cdot\left[Ze\,\nabla\langle\phi+\Phi\rangle+\mu\,\nabla B - m\Omega^2 R\,\nabla R\right] \tag{1}$$

and

$$\frac{d\mathbf{X}}{dt} = v_\parallel\mathbf{b} + \frac{1}{Ze}\left(\frac{mv_\parallel^2}{B}+\mu\right)\frac{\mathbf{B}\times\nabla B}{B^2} + \frac{\mathbf{b}\times\nabla\langle\phi+\Phi\rangle}{B} + \frac{2mv_\parallel}{ZeB}\boldsymbol{\Omega}_\perp - \frac{m\Omega^2 R}{ZeB}\mathbf{b}\times\nabla R, \tag{2}$$

where $B_\parallel^*$ of Ref. 18 is equal to B in the local model, Φ is the background potential, and $\boldsymbol{\Omega}_\perp$ is the rotation vector perpendicular to the field, i.e., $\boldsymbol{\Omega}_\perp=\boldsymbol{\Omega}-(\boldsymbol{\Omega}\cdot\mathbf{b})\mathbf{b}$. The last two terms in Eq. (2) are the Coriolis and centrifugal drifts, respectively. For the full definitions of the other symbols, we refer the reader to Ref. 18.

A. Centrifugal effect on equilibrium

The gyrokinetic equation is expanded in the small parameter $\rho_*=\rho/R\ll 1$. The local model used is congruent with the so-called δf formulation, in which the distribution function is split $F=F_M+f$ into an equilibrium part and a small time-dependent perturbation ($f\sim\rho_* F_M$). The equilibrium background distribution is assumed to be Maxwellian in velocity space

$$F_M = \frac{n}{(2\pi T/m)^{3/2}}\exp\left[-\frac{m(v_\parallel-u_\parallel)^2}{2T}-\frac{\mu B}{T}\right], \tag{3}$$

where $u_\parallel=(RB_t/B)[\omega_\phi(\psi)-\Omega]$. In the local frame chosen $u_\parallel=0$, but a constant gradient $u'=-(R_A/v_{\mathrm{th}})(\partial\omega_\phi/\partial\psi)$ in the plasma rotation is kept when derivatives of the Maxwellian are evaluated.[18] Radial variation in the plasma rotation profile is responsible for diffusive momentum transport and can alter the stability threshold for ITG modes.[26]

Starting from phase space conservation of the gyrocenter distribution $F(\boldsymbol{X},\mu,v_\parallel)$ and expanding to lowest order in ρ_*, the equilibrium equation is obtained

$$v_\parallel\boldsymbol{b}\cdot\nabla F_M - \frac{1}{m}\boldsymbol{b}\cdot\left[Ze\,\nabla\langle\Phi\rangle+\mu\,\nabla B - m\Omega^2 R\,\nabla R\right]\frac{\partial F_m}{\partial v_\parallel} = 0. \tag{4}$$

As a consequence of the centrifugal force, the background potential Φ must be retained in the equilibrium in order for quasineutrality to be satisfied.[9] For the ions, this background potential acts to detrap the particles, but is outweighed by the centrifugal force which acts to trap them. The electrons experience an enhanced trapping from the background potential.

Solving the equilibrium equation shows that in the presence of rotation the density is no longer constant over the flux surface

$$n_s(\theta) = n_{R_0,s}\exp\left[\frac{-Z_s e\langle\Phi\rangle}{T_s}+\frac{m_s\Omega^2(R^2-R_0^2)}{2T_s}\right], \tag{5}$$

where $R_0(\psi)$ is a constant of integration chosen to be the major radius at which $n(\theta)=n_{R_0}$ for *each* local flux surface. The approximation $\langle\Phi\rangle\approx\Phi$ is made, since the background potential Φ is an equilibrium quantity, with variation only over large length scales. In the rotating frame, Φ is calculated by applying the quasineutrality condition over all the species, which in the case of a pure hydrogenic plasma solves exactly to give

$$e\Phi = \frac{T_e T_i}{T_e+T_i}\left(\frac{m_i}{T_i}-\frac{m_e}{T_e}\right)\frac{\Omega^2}{2}(R^2-R_0^2). \tag{6}$$

In the general case of a multispecies plasma Φ is calculated numerically. It is convenient to combine the centrifugal force and background potential in the (species dependent) centrifugal energy

$$\mathcal{E}(\theta) = Ze\Phi - \tfrac{1}{2}m\Omega^2(R^2-R_0^2) \tag{7}$$

such that the equilibrium density variation can be written as an additional energy in the Maxwellian

$$F_M = \frac{n_{R0}}{(2\pi T/m)^{3/2}}\exp\left[-\frac{m(v_\parallel-u_\parallel)^2/2+\mu B+\mathcal{E}}{T}\right] \tag{8}$$

and $n_s(\theta,\psi)=n_{R_0,s}(\psi)\exp(-\mathcal{E}_s(\theta,\psi)/T_s(\psi))$.

It must be noted that this redistribution of density will be different for each flux surface, with the result that the density gradient will also be modified by the centrifugal force. A choice must be made of where the input density and density gradient are defined. In GKW, the numerically convenient

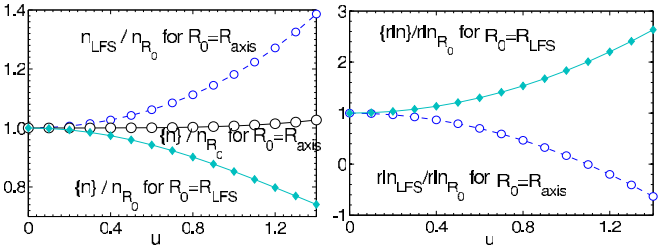

FIG. 1. (Color online) Comparison of density (left) and effective density gradient R/L_n^E (labeled *rln*, right) in a rotation scan for the GA-STD case with $R_0=R_{\text{axis}}$ (circles) and $R_0=R_{\text{LFS}}$ (diamonds). The flux surface average value is denoted by { }, and the value at the low field side midplane by LFS.

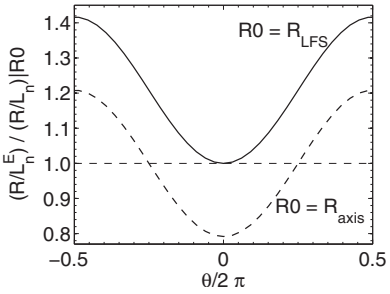

FIG. 2. Flux surface variation in effective density gradient R/L_n^E with $R_0=R_{\text{LFS}}$ (solid), and $R_0=R_{\text{axis}}$ (dashed) for $u=0.5$ and GA-STD parameters for $s-\alpha$ geometry.

choice of a single major radius R_0 at which to define n_{R_0} and $R/L_n|_{R_0}$ is used. Two options are available: the magnetic axis $R_0=R_{\text{axis}}$ and the midplane of the flux surface at the low field side $R_0=R_{\text{LFS}}$. While physical results are independent of the integration constant, the choice determines at which location the density and its gradient are held constant when scanning over rotation. The consequence of each choice for the density is shown in Fig. 1; the flux surface average density (denoted by {}) is nearly constant for $R_0=R_{\text{axis}}$, but not the density at the low field side midplane.

With the density variation over the flux surface, we define the local dimensionless density gradient as

$$\frac{R}{L_n^E}(\theta) = -\frac{1}{n}\frac{\partial n}{\partial \psi} = \frac{1}{T}\frac{\partial \mathcal{E}}{\partial \psi} + \frac{\mathcal{E}}{T}\frac{R}{L_T} + \left.\frac{R}{L_n}\right|_{R_0}, \tag{9}$$

where

$$\left.\frac{R}{L_n}\right|_{R_0} = -\frac{1}{n_{R0}}\frac{\partial n_{R0}}{\partial \psi} \tag{10}$$

is the dimensionless density gradient evaluated at R_0. Other options such as $1/\{n\}(\partial n/\partial\psi)$ or $1/n_{R_0}(\partial n/\partial\psi)$ could also be used. For the cases presented in this work, the term in Eq. (9) proportional to $\mathcal{E}$ dominates the term proportional to $\partial\mathcal{E}/\partial\psi$.

In the case of the pure hydrogenic plasma, it can be shown that $\mathcal{E}_i/T_i=\mathcal{E}_e/T_e$ (as it must be to satisfy quasineutrality) and neglecting the electron mass

$$\mathcal{E}_s = -\frac{T_s}{T_i+T_e}\frac{m_i}{2}\Omega^2(R^2-R_0^2). \tag{11}$$

The effective density gradient modification can then be shown to be

$$\frac{R}{L_n^E} - \left.\frac{R}{L_n}\right|_{R_0} = \left(\frac{\partial T_e}{\partial\psi}+\frac{\partial T_i}{\partial\psi}\right)\frac{m_i\Omega^2(R^2-R_0^2)}{2(T_e+T_i)^2} - \frac{m_i\Omega^2}{T_e+T_i}\left(R\left.\frac{\partial R}{\partial\psi}\right|_\theta - R_0\left.\frac{\partial R_0}{\partial\psi}\right|_\theta\right), \tag{12}$$

where the radial gradient of R_0 is kept in order that the density gradient keeps the usual property of being defined at constant θ. The parallel variation of R/L_n^E is plotted in Fig. 2.

For the ideal thought experiment in which rotation is varied independently of other plasma parameters, one preference might be to keep the total number of particles on a flux surface constant (the flux surface averaged density) with changing Ω. In practice, it is difficult to experimentally scan over rotation without varying the average density, and many diagnostic reconstructions use the assumption of a constant flux surface density. When studying ballooning modes in which the drive is localized on the low field side, it would be desirable to investigate the centrifugal effects irrespective of the density variation effects, in which case $R_0=R_{\text{LFS}}$ might be an appropriate choice. Since the dependencies of ITG mode and TEM turbulence on density and density gradient are well known,[27–29] we would ideally like to examine the other consequences of the centrifugal terms. To this end, the choice $R_0=R_{\text{LFS}}$ is used (unless stated otherwise) for the simulations presented here, with the assumption that it best minimizes density variation alterations to the turbulence drive (insofar as this is possible). This choice also precludes the possibility of negative R/L_n^E, since the density gradient is at its minimum at the low field side (Fig. 2). For the rotation scans presented here, differences between $R_0=R_{\text{axis}}$ and $R_0=R_{\text{LFS}}$ have little bearing on the ITG modes, and for the TEM mode are not significant below $u=0.6$.

The centrifugal force also modifies the solution of the Grad–Shafranov equation, resulting in an increased outboard compression of the flux surfaces, commonly known as the Shafranov shift. The effects of the Shafranov shift on turbulence are an already known geometry effect.[30–32] The rotational Shafranov shift scales as βu^2, and is excluded in the present work which deals with the electrostatic limit. For a complete description of all inertial effects, this effect could be included via coupling to an equilibrium solver which also includes rotation.

B. Centrifugal effects on perturbations

Starting again from phase space conservation, the gyrokinetic equation is expanded to first order in ρ_*. Neglecting the parallel velocity nonlinearity (ordering $\partial f/\partial v_\parallel \sim \rho_* \partial F_M/dv_\parallel$) and using the equilibrium condition Eq. (4) we obtain the equation for the perturbed distribution

$$\frac{\partial f}{\partial t} + \frac{d\mathbf{X}}{dt}\cdot\nabla f - \frac{\mathbf{b}}{m}\cdot(\mu\nabla B + \nabla\mathcal{E})\frac{\partial f}{\partial v_\parallel} = S, \tag{13}$$

where the source term is given by

$$S = -\mathbf{v}_E \cdot \left(\frac{\nabla n_{R_0}}{n_{R_0}} - \frac{m\Omega^2}{T} R_0 \left. \frac{\partial R_0}{\partial \psi} \right|_\theta \nabla \psi \right.$$
$$\left. + \left[\frac{v_\parallel^2}{v_{\rm th}^2} + \frac{(\mu B + \mathcal{E})}{T} - \frac{3}{2} \right] \frac{\nabla T}{T} + \frac{m v_\parallel R B_t}{BT} \nabla \omega_\phi \right) F_M$$
$$- \frac{Ze}{T} \frac{d\mathbf{X}}{dt} \cdot \nabla \langle \phi \rangle F_M. \quad (14)$$

The additional appearance of $\partial R_0/\partial\psi$ when compared to Ref. 18 is due to the allowance for the case $R_0 = R_{\rm LFS}$. When $R_0 = R_{\rm axis}$, $\partial R_0/\partial\psi|_\theta = 0$ in the $s-\alpha$ model equilibrium.

Finally, the gyrokinetic Poisson equation of Ref. 25 is modified in the polarization term by the inclusion of the density variation in the Maxwellian (this was not discussed in Ref. 18)

$$\sum_s Z_s n_{R_0,s} \left(2\pi B \int dv_\parallel d\mu J_0(k_\perp \rho_s) \hat{f}_s \right.$$
$$\left. + \frac{Z_s}{T_s} [\Gamma(b_s) - 1] \exp(-\mathcal{E}_s/T_s) \hat{\phi} \right) = 0, \quad (15)$$

where

$$b = \frac{1}{2} \frac{k_\perp^2 m_s^2 v_{{\rm th},s}^2}{e^2 B^2}. \quad (16)$$

For complete definitions of all quantities, we refer the reader to Ref. 25. The modification to the polarization term only becomes important at small wavelengths ($k_\perp \rho_s > 1$).

In the limit of an adiabatic electron response the Poisson equation becomes

$$\sum_{s,\rm ions} Z_s n_{R_0,s} \left(2\pi B \int dv_\parallel d\mu J_0(k_\perp \rho_s) \hat{f}_s \right.$$
$$\left. + \frac{Z_s}{T_{Rs}} [\Gamma(b_s) - 1] \exp(-\mathcal{E}_s/T_s) \hat{\phi} \right)$$
$$= \frac{n_{R_0,e} \exp(-\mathcal{E}_e/T_e)}{T_{Re}} (\hat{\phi} - \{\widehat{\phi}\}), \quad (17)$$

where the index e refers to the electrons, and the sum on the left hand side of the equation is over all ion species.

Equations (2), (8), and (13)–(15) together form the complete set of electrostatic collisionless gyrokinetic equations solved by the code for the cases presented in this work, and contain all the modifications arising from the inclusion of the centrifugal force.

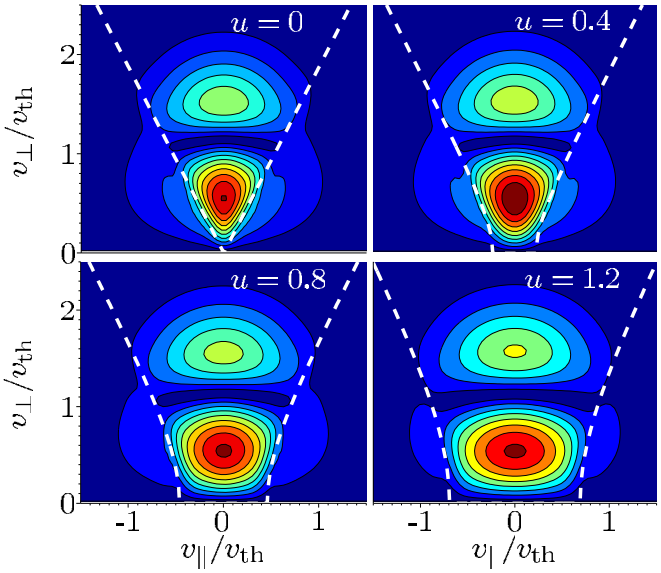

FIG. 3. (Color online) Magnitude of perturbed electron distribution in velocity space for the GKW-TEM case at the outboard midplane with increasing rotation. Arbitrary units and contours are equally spaced at same intervals for each plot. The trapping boundary of Eq. (18) is overplotted as a dashed line.

The modification to the trapping term in Eq. (13) means that particles are trapped if

$$v_\perp^2 > \frac{v_\parallel^2 - \frac{2}{m}(\mathcal{E}_H - \mathcal{E}_L)}{\frac{B_H}{B_L} - 1}, \quad (18)$$

where the subscripts H and L refer to the high and low field sides, respectively. Example evaluations of the modified trapping condition are overplotted in Fig. 3.

Using Eq. (11) and the simplification of concentric circular flux surfaces the trapping condition for both species becomes

$$\frac{v_{\perp,s}^2}{v_{{\rm th},s}^2} > \left(\frac{v_{\parallel,s}^2}{2\epsilon v_{{\rm th},s}^2} - \frac{2T_i}{T_i + T_e} u^2 \right) (1 - \epsilon), \quad (19)$$

where $\epsilon = r/R_A = \psi$ is the inverse aspect ratio of the flux surface. We point out that the enhanced trapping on the electrons is due to the background potential, not the direct effect of the centrifugal force on the electrons. For the ions, the combination of the detrapping from the background potential and the trapping from the centrifugal force partially cancel, resulting in the identical trapping condition (and trapped fraction) for both species.

C. Summary of inertial terms

To better analyze the effect of the inertial forces, for convenience we divide the additional terms in the equations into three categories:

(1) (TR) All consequences arising from the parallel component of the centrifugal force, as expressed in the centrifugal potential Φ and the centrifugal energy $\mathcal{E}$.

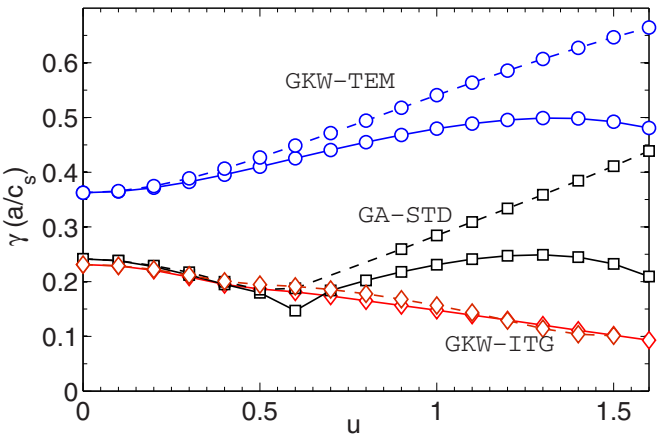

FIG. 4. (Color online) Mode growth rate against rotational Mach number for the GA-STD (squares), GKW-ITG (diamonds), and GKW-TEM (circles) cases, for both $R_0=R_{\text{axis}}$ (solid) and $R_0=R_{\text{LFS}}$ (dashed).

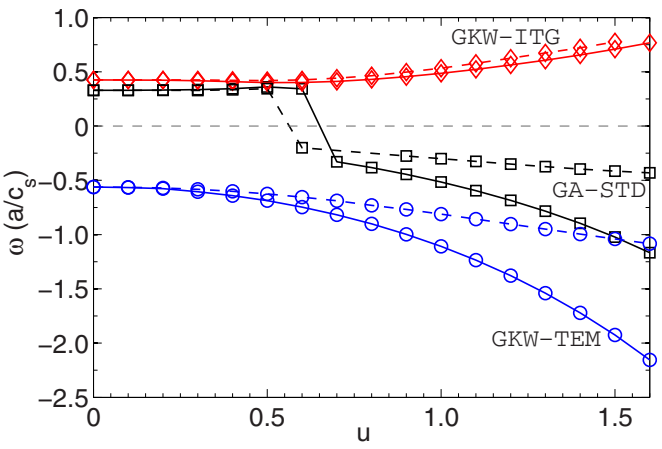

FIG. 5. (Color online) Mode frequencies in the comoving frame for the three cases, for both $R_0=R_{\text{axis}}$ (solid) and $R_0=R_{\text{LFS}}$ (dashed). Positive values of ω indicate propagation in the ion diamagnetic direction. The GA-STD case clearly shows the transition from ITG mode to TEM.

This includes the density variation in the Maxwellian, the modification to the source S, the mirror force on the perturbed distribution $\boldsymbol{b}\cdot\nabla\mathcal{E}(\partial f/\partial v_{\parallel})$, the drift $(\boldsymbol{b}\times\nabla\Phi/B)\cdot\nabla f$ in the perturbed distribution, and the modification to the polarization. For brevity we later refer to this group of effects as the "trapping terms."

(2) (CF) The centrifugal drift: $\boldsymbol{v}_{\text{cf}}=-(m\Omega^2R/ZeB)\boldsymbol{b}\times\nabla R$ arising from the perpendicular component of the centrifugal force.

(3) (CO) The Coriolis drift: $\boldsymbol{v}_{\text{co}}=(2mv_{\parallel}/ZeB)\boldsymbol{\Omega}_{\perp}$. The effect of this term (particularly with regards to momentum transport) has previously been discussed in detail[20–23] and while included in these simulations is not discussed at length in this work.

Finally, the heat fluxes are defined as

$$Q=\left\{\int d^3\mathbf{v}\tilde{\mathbf{v}}_E\cdot\nabla\psi\frac{mv^2}{2}f\right\} \tag{20}$$

which upon transformation to the comoving frame are related to the fluxes in the laboratory frame by

$$Q^*=Q^L-m\frac{RB_t}{B}\Omega\Gamma^L_{\phi}+\frac{1}{2}mR^2\Omega^2\frac{B_t}{B}\Gamma^L, \tag{21}$$

where $*$ denotes the comoving frame, L is the laboratory frame, Γ is the particle flux, and Γ_{ϕ} is the flux of toroidal momentum. The fluxes presented in this work are all fluxes calculated in the rotating frame, but are similar to those in the laboratory frame since Γ^L_{ϕ} and $\Gamma^L=\Gamma^*$ are small for typical simulation parameters.

TABLE I. Parameters for the three linear cases studied.

Case	$k_{\theta}\rho_s$	R/L_{T_i}	R/L_{T_e}
GA-STD	0.304	9.0	9.0
GKW-ITG	0.304	9.0	1.0
GKW-TEM	0.707	1.0	9.0

III. SYSTEM DESCRIPTION

Results are presented in the standard gyro-Bohm units in which a is the plasma minor radius, $c_s=\sqrt{T_e/m_i}$ is the ion sound speed, $\rho_s=c_s/\omega_{ci}$ is the ion-sound Larmor radius, and $\omega_{ci}=eB/m_i$ is the ion cyclotron frequency evaluated on the magnetic axis.

We examine the collisionless Waltz standard case[33] (which we label GA-STD) of a deuterium plasma with $R/L_T=9$, $R/L_n=3$, $R/a=3$, electron to ion temperature ratio $T_e/T_i=1$, mass ratio $\sqrt{(m_i/m_e)}=60$, safety factor $q=2$, magnetic shear $\hat{s}=1$, and inverse aspect ratio $\epsilon=1/6$. Except where stated otherwise, the geometry used is the $s-\alpha$ model, which assumes circular flux surfaces with the magnetohydrodynamics parameter $\alpha=0$, with geometry quantities evaluated to only lowest order in ϵ.

In addition to the GA-STD case, we examine a pure TEM case (labeled GKW-TEM) and a pure ITG mode case (labeled GKW-ITG). The cases all use the parameters above, and differ only as listed in Table I.

The wavenumber $k_{\theta}\rho_s=0.304$ studied is the most unstable part of the ITG branch at zero rotation, while a higher wavenumber $k_{\theta}=0.707$ is chosen for the TEM case, typical of the wavelengths at which TEMs start to dominate ITG modes at zero rotation.

Except where stated otherwise, the simulations are performed for a single field line with five poloidal turns (equivalent to a single turn with five radial wavenumbers) and all calculations are performed with kinetic electrons. For the linear spectrum calculations of Figs. 6 and 7, the results presented are matched as closely as possible to the nonlinear cases presented later. The results presented therefore use a circular geometry model[34] (for reasons made clear later), and a single field line with 25 poloidal turns.

IV. LINEAR RESULTS

A. Stability analysis

In this section we examine the effect of the rotation on the linear stability and frequency of the ITG mode and TEM

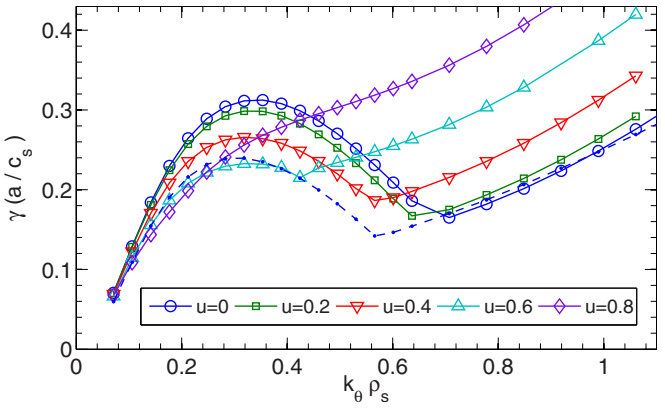

FIG. 6. (Color online) Growth rate spectrum for the GA-STD case at various bulk ion Mach numbers. The results shown use the circular geometry model with 25 poloidal turns (dashed line is $s-\alpha$ geometry, with $u=0.0$).

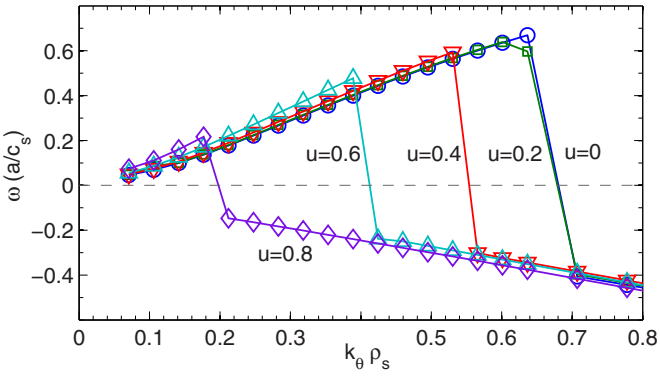

FIG. 7. (Color online) Dispersion relation for the GA-STD case at various bulk ion Mach numbers. The TEM and ITG branches have been left artificially connected to highlight the shift of TEM dominance to longer wavelengths with increasing rotation. Positive values of ω indicate propagation in the ion diamagnetic direction and frequencies are evaluated in the comoving frame. The results shown use the circular geometry model with 25 poloidal turns.

drift waves. First, we examine the growth rate of the modes for the three cases (Fig. 4). As expected, the effect of the inertial terms is small at low Mach numbers. The ITG mode instability is stabilized by higher Mach numbers while the TEM is enhanced. The enhancement of the TEM is due to the enhanced mirror force which adds to the trapping condition independently of position in $v_\perp$ space, widening the base of the trapping region. The increased phase space from which the mode can tap energy results in the increased growth rate. This can be clearly seen in the velocity space of the perturbed electron distribution for the GKW-TEM case (Fig. 3) which exactly matches the trapping condition of Eq. (18).

For the more physically realistic equal temperature gradients of the GA-STD case, the suppression of the ITG branch and the enhancement of the TEM branch leads to a transition threshold at around $u=0.6$ after which the TEM becomes dominant over the ITG mode. At the transition, the direction of mode propagation reverses, as shown in the reversal of the mode frequency (Fig. 5). From these results, it is clear that the choice of $R_0=R_{\text{axis}}$ or $R_0=R_{\text{LFS}}$ only becomes important at high Mach numbers and is only of importance for the TEM branch. Previous work has shown that ITG mode stability [Fig. 5(a) of Ref. 33] is less sensitive to density and density gradient variations than TEM stability,[28,29] although the propagation frequencies of both show some variation with R/L_n.

The wavenumber $k_\theta\rho_s=0.304$ studied is the most unstable part of the ITG mode spectrum at zero rotation (Fig. 6), but at shorter wavelengths the TEM is dominant. Identifying which branch is dominant at a given wavenumber follows from the dispersion relation (Fig. 7). It is clear from Fig. 7 that the TEM instability becomes dominant at ever larger wavelengths with increasing rotation. Our results show that the transition threshold is sensitive to the geometry, length of field line resolved, and parallel velocity dissipation.

We next discuss further the suppression of the ITG branch by examining the effect of each of the inertial terms independently and in combination. We divide the rotational effects into three as discussed in Sec II C. Simulations of the GKW-ITG and GKW-TEM cases were performed with each of the inertial terms artificially included or excluded (Fig. 8).

For the ITG mode, the results show that the trapping and density redistribution in isolation destabilize the mode for $u<1$. The Coriolis drift and the centrifugal drift both have a stabilizing influence at very high Mach number, which together are sufficient to overcome the destabilizing effect of the trapping terms to result in the net ITG mode stabilization when all rotational terms are kept.

For the TEM, the effect of each of the individual terms is qualitatively similar. The stabilizing influence of the centrifugal drift is outweighed by the destabilization from the trapping terms, with the result that the overall effect of all the rotational terms is to destabilize the mode.

For both the ITG mode and TEM, the Coriolis terms introduce an asymmetry in the parallel potential eigenfunction,[23] but the eigenfunction is not strongly modified by the centrifugal terms. Perturbed density eigenfunctions are shown in Fig. 11, which for the bulk ions closely follow the potential eigenfunction.

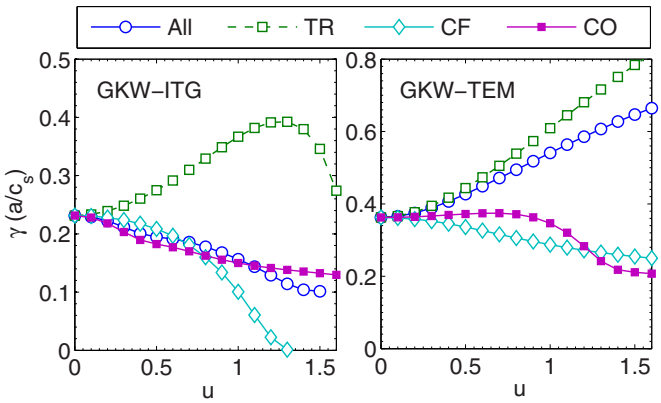

FIG. 8. (Color online) Effect of individual inertial terms for the GKW-ITG and GKW-TEM cases on mode growth rate: centrifugal trapping and potential (TR), centrifugal drift (CF), and Coriolis drift (CO).

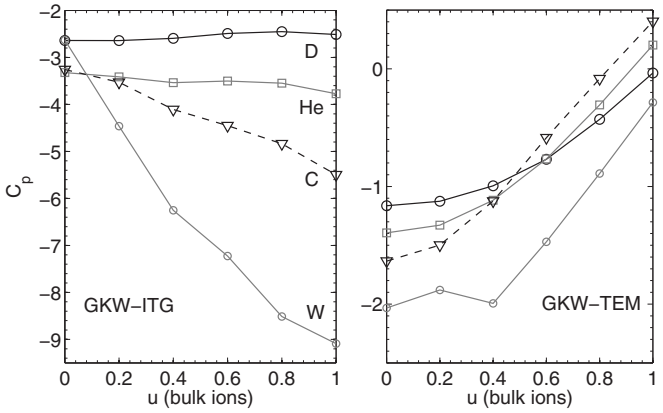

FIG. 9. Convective coefficient C_p for trace species deuterium, helium, carbon, and tungsten for GKW-ITG and GKW-TEM cases both with $k_\theta \rho_s = 0.304$. Symbols for each species are the same on both graphs.

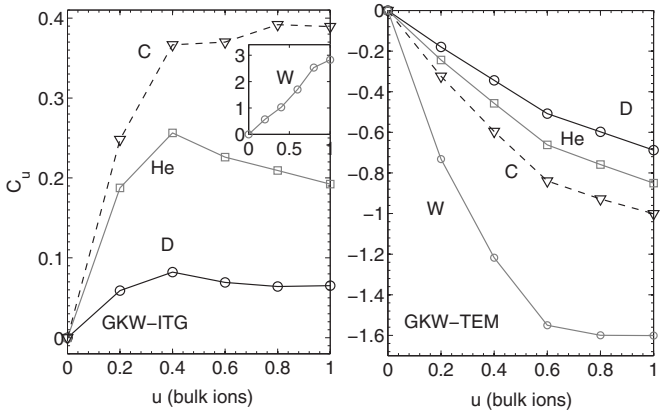

FIG. 10. Rotodiffusive coefficient C_u for trace species deuterium, helium, carbon, and tungsten for GKW-ITG and GKW-TEM cases both with $k_\theta \rho_s = 0.304$.

B. Particle and impurity transport

Heavy impurity ions have higher relative Mach numbers due to their lower thermal velocity, and it is therefore expected that the centrifugal effects will be felt strongly by heavy impurities even at low Mach number u of the bulk ions. To investigate the effect of plasma rotation on particle and impurity transport, linear simulations with a number of trace ion species (which do not affect the properties of the mode solution) are conducted. The trace species do not contribute to the solution of the Poisson equation Eq. (15), with the result that the particle flux of the trace becomes linear in the trace species gradients. The turbulent particle flux for each species can then be divided into four components

$$\Gamma_s = n_s D_s \left(\left. \frac{R}{L_n} \right|_{R_0} + C_T \frac{R}{L_T} + C_u u' + C_p \right) \tag{22}$$

which are the diffusive part, the thermodiffusive part, the rotodiffusive part, and the convective part, respectively.[23,35,36]

The magnitude of the particle fluxes can only be quantified by nonlinear simulations of the saturated turbulent state. In linear simulations, the fluxes grow exponentially, but variations in the dimensionless ratios C_p, C_T, and C_u may be estimated without the nonlinear saturation of the fluxes. Since the cross-phase of the perturbed potential with density or temperature observed in nonlinear simulations shows similarity with that of linear simulations,[28] the dimensionless parameters are expected to follow the same trends in linear and nonlinear simulations. For a stationary plasma without any particle source, $\Gamma = 0$, so that in the case of negligible neoclassical transport $-C_T$, $-C_u$, and $-C_p$ give a measure of the steady state density gradient that may be sustained by each component.

The parameters for the bulk ions and electrons are those of the GKW-ITG and GKW-TEM cases, where the wavenumber for the GKW-TEM is modified to $k_\theta \rho_s = 0.304$, the same as for the GKW-ITG case. For the simulations presented in this section, the number of poloidal turns of the field line was increased to nine. The species simulated are deuterium (D: $Z=1$, $M_R=1$), helium (He: $Z=2$, $M_R=1.987$), carbon (C: $Z=6$, $M_R=5.964$), and partially ionized tungsten (W: $Z=46$, $M_R=91.28$). For each ion, three trace species $T1$, $T2$, and $T3$ are included with equilibrium gradients $(R/L_n|_{R_0}=10,\ R/L_T=0,\ u'=0)$, $(R/L_n|_{R_0}=0,\ R/L_T=0,\ u'=0)$, and $(R/L_n|_{R_0}=0,\ R/L_T=0,\ u'=10)$, respectively. All species have the same temperature as the bulk ions, and rotate with the same velocity (neoclassical effects are neglected).

The coefficients C_p (Fig. 9) and C_u (Fig. 10) are then calculated as

$$C_p = \frac{\Gamma_{T2}}{\Gamma_{T1} - \Gamma_{T2}} \left. \frac{R}{L_n} \right|_{R_0}, \tag{23}$$

$$C_u = \frac{\Gamma_{T3} - \Gamma_{T2}}{u'(\Gamma_{T1} - \Gamma_{T2})} \left. \frac{R}{L_n} \right|_{R_0}. \tag{24}$$

For the GKW-ITG case, the convective impurity pinch $-C_p$ increases with the rotation, more strongly with increasing impurity mass. For the GKW-TEM case, the inertial terms reduce the convective pinch, with less dependence on the impurity mass. For the rotodiffusive coefficient C_u, the behavior for the tungsten impurity is qualitatively different to the other ions, this we attribute to the different charge to mass ratio of the partially ionized impurity. The results show that the rotodiffusive coefficient C_u is small compared to C_p for the GKW-ITG case, while in the GKW-TEM case, the magnitude of the effect for the centrifugal terms is comparable to that for the convective part. Inclusion of additional species with $R/L_T > 0$ indicates that the thermodiffusive part C_T (which is unimportant for heavy impurities[36]) is unaffected by the rotation, and is not presented here.

The effects of the inertial terms on these convective coefficients are in good agreement with the predictions of the low field side fluid model of Ref. 23. In the present simulations, there is a modification to the mode frequency from the inertial terms (Fig. 5), and a modification to the trapping and velocity space structure (Fig. 3), both of which play a role in determining the particle transport.[23,36] The parallel mode structure of the potential and bulk ions (Fig. 11) is largely unaffected by the centrifugal terms, and trace impurities play

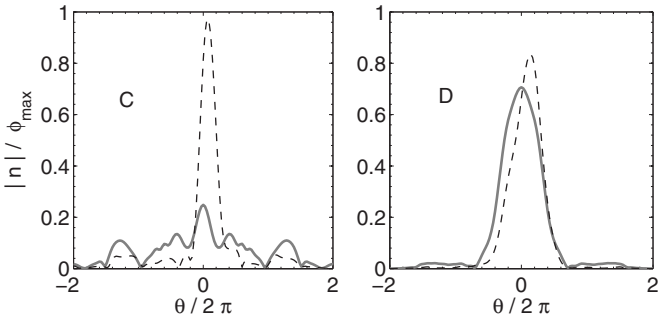

FIG. 11. Perturbed ion density parallel eigenfunctions for the GA-STD case with $u=0$ (solid) and $u=0.6$ (for the bulk ions) (dashed) for carbon and deuterium traces.

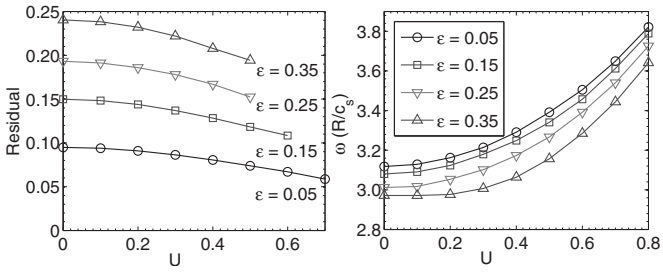

FIG. 12. Zonal flow residual $\phi(t=\infty)/\phi(t=0)$ and GAM frequency for $q=1.1$.

no role in the potential eigenfunction. Calculations of the parallel potential wavenumber show that the predictions of Ref. 23 (which depend on $k_\parallel$ and $k_\parallel^2$ of the potential eigenfunction only) are not significantly altered by any modification to the mode structure resulting from the centrifugal terms. Asymmetry arising from the Coriolis drift results in a small $k_\parallel$ in the potential eigenfunction, but its impact on particle transport is small. Comparison with Eqs. 26 and 27 of Ref. 23 using the mode structure ($k_\parallel$ and ω) from the present gyrokinetic simulations shows close agreement. For the heavier impurities, the present GKW-ITG results predict a larger $-C_p$ (90% larger for tungsten) due to the strong trapping of the impurity not included in the fluid model (Fig. 11), since the trapped impurity ions contribute an inward flux for this case.

The model of Eq. (22) for particle transport has been developed under the assumption that all the gradient quantities in the equation are flux functions, with the fluxes and coefficients taken to be flux surface averages. We stress however, that the assumption of constant gradients is violated for heavy impurities, with the strong redistribution of density over the flux surface with rotation resulting in a coupling of the terms. Here, we have calculated the coefficients using the decomposition of this model, and used a large $R/L_n|_{R_0}$ to minimize complications in estimating the diffusive component arising from rotational variations in R/L_n^E. With large $R/L_n|_{R_0}$, we find $R/L_n|R_0 \approx R/L_n^E$ and we use $R/L_n|R_0$ for calculating the diffusion coefficient D. The results presented here should therefore be interpreted with caution: They merely make predictions about the variation with rotation of the convective and rotodiffusive particle fluxes. Future progress will require careful thought on how best to extend this model to impurities in rotating plasmas so that the diffusive coefficient can be defined and determined independently of variations in the density gradients in flux surface. Determination of realistic equilibrium impurity density gradients may involve an iterative search for zero flux states.

C. Zonal flow response

In the drift wave zonal flow paradigm, gyrokinetic turbulence is regulated by zonal flows driven through nonlinear interactions.[33,37,38] The $\boldsymbol{E}\times\boldsymbol{B}$ shear of these zonal flows acts to break apart the largest scale structures, creating a self-regulating feedback which determines the level of transport. Furthermore, since zonal flows do not contribute to radial transport, they provide a benign repository for turbulent energy. Accurate calculation of the zonal flow response is therefore vital for determining the correct turbulence saturation level.[39] At low q, an initial perturbation in a zonal mode is kinetically damped to a nonzero residual zonal flow that is independent of the initial perturbation.[40]

The inertial terms are expected to modify the zonal flow response at high rotation since the centrifugal drift modifies mode oscillation frequencies.[18] To investigate this, simulations with adiabatic electrons were used to calculate the zonal flow residual for the electrostatic collisionless case with $q=1.1$, $k_\psi\rho_s=0.0525$, for a range of ϵ and u.

Rather large grid sizes are used to avoid the recurrence problem.[41] Also for reasons of numerical stability, the circular geometry model of Ref. 34 was used, since we find it addresses some deficiencies of the standard $s-\alpha$ model which contribute to numerical instability for the zonal modes.

The results show that the residual zonal flow decreases with increasing rotation (Fig. 12), which would indicate that saturation level of turbulent fluctuations should increase with strong rotation. Numerical experiments switching off the trapping terms and drift terms independently indicates that the reduction in the residual is due to the drifts, while the trapping terms and density redistribution increase the residual by a smaller amount. The choice of $R_0=R_{\mathrm{LFS}}$ or $R_0=R_{\mathrm{axis}}$ makes no difference to the final result of (Fig. 12). The frequency of the GAM is found to increase with rotation due to the influence of the centrifugal drift. Analytic work calculating the influence of the inertial terms on the zonal response would be of interest for comparison, but is beyond the scope of the present work.

V. NONLINEAR RESULTS

Nonlinear kinetic simulations are presented for the GA-STD case. In the nonlinear phase, the GA-STD case is an ITG dominated case, with an additional drive from the trapped electrons, a scenario typical for many tokamak operating regimes.

The simulations were performed with $N_{\mathrm{mod}}=21$ binormal modes and $N_x=167$ radial modes with a perpendicular simulation domain of extent $[L_{\mathrm{radial}}, L_{\mathrm{bi\text{-}normal}}]=[120, 126]\rho_s$. The maximum resolved wavevector has binormal wavenumber $k_\theta\rho_s=1.0$, The number of grid points in parallel velocity,

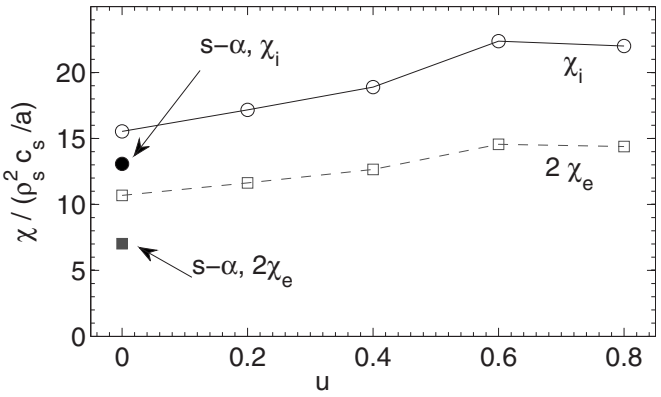

FIG. 13. Ion and electron heat diffusivities for the GA-STD case. The filled points show the equivalent result in the $s-\alpha$ geometry.

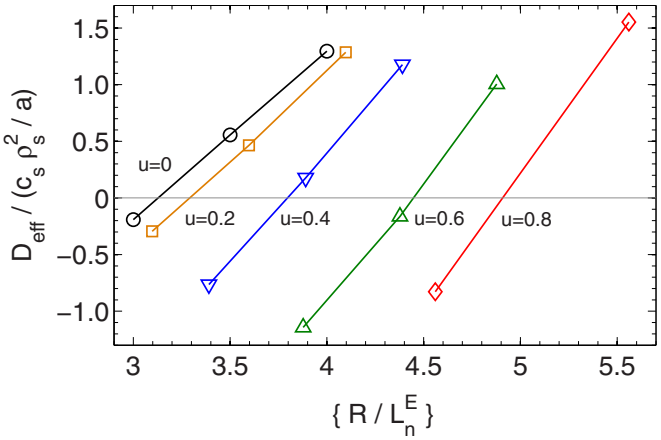

FIG. 15. (Color online) Location of zero particle flux state for GA-STD case with effective particle diffusivity calculated as $D_{\text{eff}}=\Gamma/\{R/L_n^E\}$.

magnetic moment, and along the field line are $N_{v\|}=48$, $N_\mu=8$, and $N_s=21$, respectively. These grid sizes have proved sufficient to resolve the diffusivities presented here, which are averaged for $t_{\text{av}}=550(a/c_s)$ after the saturated state was reached. The large parallel velocity resolution is used to resolve the trapped-passing boundary, required for an accurate determination of the particle flux. The circular geometry model[34] was used, to prevent numerical instabilities developing in the zonal mode, as discussed above.

The results show a moderate increase in ion heat diffusivity with rotation (Fig. 13), reaching 40% by $u=0.6$. We attribute this increase primarily to the increased trapped electron drive, but also to the decreased stabilizing response of the zonal flow. As rotation increases, we find that the magnitude of the perturbation in the zonal modes becomes less relative to the other modes. The increase in heat transport comes from the largest scales modes (Fig. 14) which are stabilized most by the zonal flow. The promotion of the TEMs shown in the linear results leads to an increase in electron heat transport at smaller scales (Fig. 14), but since these scales contribute little to overall transport, the result is that the electron heat transport shows no more increase than the ion heat transport. Comparing the linear mode frequencies (Fig. 7) directly against transport spectrum (Fig. 14), we note that mode propagation is in the ion direction at the scales which the dominate the transport for all values of rotation simulated. A transition to TEM dominance might be expected for a case less dominated by ITG transport (with $(R/L_{T_e})/(R/L_{T_i})>1$ and $\chi_i\approx\chi_e$), in which the electron heat transport may show a marked increase with Mach number. The linear results suggest that such a transition would be sensitive to collisionality and geometry, and further investigation we leave for a later work.

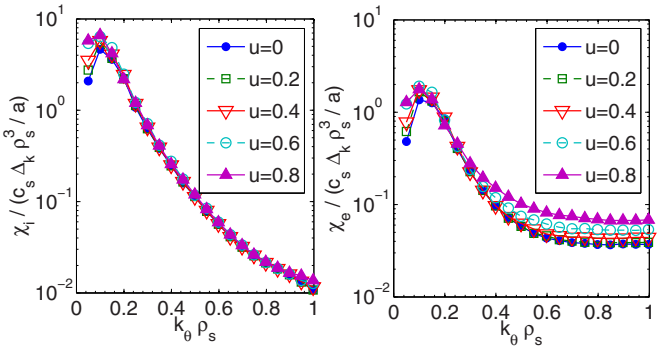

FIG. 14. (Color online) Spectral ion (left) and electron (right) heat diffusivities for the GA-STD case.

It is necessary to point out that in practice an increased toroidal rotation will often be associated with an increased toroidal rotation gradient, which is not included in the present simulations. The stabilizing effect of the $\boldsymbol{E}\times\boldsymbol{B}$ shear from the perpendicular component competes against the destabilizing effect of the parallel velocity shear[26] and is sensitive to geometry parameters q and ϵ. For the GA-STD case, the effects are well balanced,[42,43] but for other cases the stabilizing effect of $\boldsymbol{E}\times\boldsymbol{B}$ shear can dominate[44] and would counter the increased transport predicted by Fig. 13.

When investigating the effect of rotation on particle transport, it is particularly important to be mindful of the previously discussed coupling of the rotation and density gradient. In order to examine a quantity with physical meaning that is independent of definitions of the density gradient, we searched for the null particle flux state ($\Gamma=0$), varying $R/L_n|_{R_0}$ between three and four. The results in Fig. 15 are plotted against the flux surface average $\{R/L_n^E\}$ since it is independent of the R_0 used, and is most relevant in determining the central density linked to fusion performance. The total particle flux is determined by the balance between an inward contribution from low energy trapped electrons, and an outward contribution from higher energy trapped electrons.[36] These results indicate that for the GA-STD case (ITG turbulence dominated), the increased fraction of low energy trapped electrons (Fig. 3) due to the centrifugal trapping lead to an increase in the steady state $\{R/L_n^E\}$ with increasing rotation. Collisions are also known to play a role in determining particle transport by similarly altering the balance between trapped and passing electrons.[36] Preliminary nonlinear simulations with collisions show that the increase in the particle pinch due to the rotational mode rebalancing persists at the same magnitude; full nonlinear investigation of particle and impurity transport with collisions we leave for a later work.

VI. CONCLUSIONS

The gyrokinetic equations formulated in a comoving frame that rotates with the plasma[18] allow for natural inclusion of the centrifugal and Coriolis forces in a local flux tube model. This work describes the implementation of these inertial terms in the gyrokinetic code GKW, and presents the first gyrokinetic simulations including the centrifugal force, relevant to the case of a strongly rotating plasma.

The parallel component of the centrifugal force redistributes equilibrium density over the flux surface and causes an enhanced mirror force which enlarges the trapped particle region in velocity space (Fig. 3). The extended trapping region alters the threshold for the TEM, promoting it over the ITG mode at intermediate scales (Fig. 7). The perpendicular component of the centrifugal force results in the centrifugal drift, which modifies the mode frequency, and reduces the residual of the zonal flow response (Fig. 12).

Nonlinear simulations of ITG mode dominated turbulent transport indicate a moderate increase in the ion heat diffusivity with strong rotation (Fig. 13) due to the increased trapped electron drive and reduced regulation from the zonal flow. These simulations considered rotation, but did not include the stabilizing effect of rotational shear. For cases which are less dominated by the ITG driven modes, it is expected that electron heat transport will show a marked increase with rotation, as the TEM becomes dominant at the scales of maximum transport.

Increased numbers of slow trapped electrons enhance the convective particle pinch[35] in the nonlinear simulations, resulting in an increased steady state density gradient with rotation (Fig. 15). These results suggest that strong rotation could impact core particle density, with possible benefits for fusion performance. Preliminary linear investigations into trace impurity transport for the ITG show a stronger convective pinch for heavy impurities due to their strong centrifugal trapping (Fig. 9). For heavy impurities, the redistribution of equilibrium density over the flux surface due to the centrifugal force is extreme, resulting in strong modifications to the diffusive particle flux. Determination of steady state impurity gradients in the presence of rotation will require further investigation, with nonlinear simulations including the effect of collisions needed to quantify the behavior of turbulent impurity transport in a rotating plasma.

ACKNOWLEDGMENTS

We are grateful to the referee for two careful readings of the manuscript which caught a number of errors in the equations. F.J.C. would also like to thank K. G. McClements, P. DeVries, and W. Guttenfelder for interesting discussions.

This work was funded by EPSRC in association with CCFE and simulations were performed using the HPC-FF resource at the Jülich Supercomputing Centre (projects FSCFIM/FSCENU) and the HECTOR U.K. national resource (project EP/H002081/1).

[1] H. Biglari, P. H. Diamond, and P. W. Terry, Phys. Fluids B **2**, 1 (1990).
[2] R. C. Wolf, Plasma Phys. Controlled Fusion **45**, R1 (2003).
[3] A. Bondeson and D. J. Ward, Phys. Rev. Lett. **72**, 2709 (1994).
[4] L.-G. Eriksson, E. Righi, and K.-D. Zastrow, Plasma Phys. Controlled Fusion **39**, 27 (1997).
[5] J. Rice, A. Ince-Cushman, J. deGrassie, L.-G. Eriksson, Y. Sakamoto, A. Scarabosio, A. Bortolon, K. Burrell, B. Duval, C. Fenzi-Bonizec, M. Greenwald, R. Groebner, G. Hoang, Y. Koide, E. Marmar, A. Pochelon, and Y. Podpaly, Nucl. Fusion **47**, 1618 (2007).
[6] P. de Vries, M. Hua, D. McDonald, C. Giroud, M. Janvier, M. Johnson, T. Tala, and K. Zastrow, Nucl. Fusion **48**, 065006 (2008).
[7] R. J. Akers, J. W. Ahn, G. Y. Antar, L. C. Appel, D. Applegate, C. Brickley, C. Bunting, P. G. Carolan, C. D. Challis, N. J. Conway, G. F. Counsell, R. O. Dendy, B. Dudson, A. R. Field, A. Kirk, B. Lloyd, H. F. Meyer, A. W. Morris, A. Patel, C. M. Roach, V. Rohzansky, A. Sykes, D. Taylor, M. R. Tournianski, M. Valovič, H. R. Wilson, K. B. Axon, R. J. Buttery, D. Ciric, G. Cunningham, J. Dowling, M. R. Dunstan, S. J. Gee, M. P. Gryaznevich, P. Helander, D. L. Keeling, P. J. Knight, F. Lott, M. J. Loughlin, S. J. Manhood, R. Martin, G. J. McArdle, M. N. Price, K. Stammers, J. Storrs, M. J. Walsh, MAST, and NBI Team, Plasma Phys. Controlled Fusion **45**, A175 (2003).
[8] S. Kaye, W. Solomon, R. Bell, B. LeBlanc, F. Levinton, J. Menard, G. Rewoldt, S. Sabbagh, W. Wang, and H. Yuh, Nucl. Fusion **49**, 045010 (2009).
[9] F. L. Hinton and S. K. Wong, Phys. Fluids **28**, 3082 (1985).
[10] S. K. Wong, Phys. Fluids **30**, 818 (1987).
[11] P. J. Catto, I. B. Bernstein, and M. Tessarotto, Phys. Fluids **30**, 2784 (1987).
[12] H. Sugama and W. Horton, Phys. Plasmas **4**, 2215 (1997).
[13] R. D. Hazeltine and F. L. Hinton, Phys. Plasmas **12**, 102506 (2005).
[14] K. G. McClements and R. J. McKay, Plasma Phys. Controlled Fusion **51**, 115009 (2009).
[15] E. A. Belli and J. Candy, Plasma Phys. Controlled Fusion **51**, 075018 (2009).
[16] A. Brizard, Phys. Plasmas **2**, 459 (1995).
[17] M. Artun and W. M. Tang, Phys. Plasmas **1**, 2682 (1994).
[18] A. G. Peeters, D. Strintzi, Y. Camenen, C. Angioni, F. J. Casson, W. A. Hornsby, and A. P. Snodin, Phys. Plasmas **16**, 042310 (2009).
[19] A. Thyagaraja and K. McClements, Phys. Plasmas **16**, 092506 (2009).
[20] A. G. Peeters, C. Angioni, and D. Strintzi, Phys. Rev. Lett. **98**, 265003 (2007).
[21] A. G. Peeters, C. Angioni, Y. Camenen, F. J. Casson, W. A. Hornsby, A. P. Snodin, and D. Strintzi, Phys. Plasmas **16**, 062311 (2009).
[22] N. Kluy, C. Angioni, Y. Camenen, and A. G. Peeters, Phys. Plasmas **16**, 122302 (2009).
[23] Y. Camenen, A. G. Peeters, C. Angioni, F. J. Casson, W. A. Hornsby, A. P. Snodin, and D. Strintzi, Phys. Plasmas **16**, 012503 (2009).
[24] A. G. Peeters and D. Strintzi, Phys. Plasmas **11**, 3748 (2004).
[25] A. G. Peeters, Y. Camenen, F. J. Casson, W. A. Hornsby, A. P. Snodin, D. Strintzi, and G. Szepesi, Comput. Phys. Commun. **180**, 2650 (2009).
[26] A. G. Peeters, C. Angioni, and ASDEX Upgrade Team, Phys. Plasmas **12**, 072515 (2005).
[27] R. E. Waltz, G. D. Kerbel, J. Milovich, and G. W. Hammett, Phys. Plasmas **2**, 2408 (1995).
[28] T. Dannert and F. Jenko, Phys. Plasmas **12**, 072309 (2005).
[29] A. G. Peeters, C. Angioni, M. Apostoliceanu, F. Jenko, and F. Ryter, and ASDEX Upgrade Team, Phys. Plasmas **12**, 022505 (2005).
[30] R. E. Waltz and R. L. Miller, Phys. Plasmas **6**, 4265 (1999).
[31] E. J. Synakowski, S. H. Batha, M. A. Beer, M. G. Bell, R. E. Bell, R. V. Budny, C. E. Bush, P. C. Efthimion, T. S. Hahm, G. W. Hammett, B. LeBlanc, F. Levinton, E. Mazzucato, H. Park, A. T. Ramsey, G. Schmidt, G. Rewoldt, S. D. Scott, G. Taylor, and M. C. Zarnstorff, Phys. Plasmas **4**, 1736 (1997).
[32] C. Bourdelle, W. Dorland, X. Garbet, G. W. Hammett, M. Kotschenreuther, G. Rewoldt, and E. J. Synakowski, Phys. Plasmas **10**, 2881 (2003).
[33] R. E. Waltz, G. D. Kerbel, and J. Milovich, Phys. Plasmas **1**, 2229 (1994).
[34] X. Lapillonne, S. Brunner, T. Dannert, S. Jolliet, A. Marinoni, L. Villard, T. Görler, F. Jenko, and F. Merz, Phys. Plasmas **16**, 032308 (2009).
[35] C. Angioni and A. G. Peeters, Phys. Rev. Lett. **96**, 095003 (2006).
[36] C. Angioni, J. Candy, E. Fable, M. Maslov, A. G. Peeters, R. E. Waltz, and H. Weisen, Phys. Plasmas **16**, 060702 (2009).
[37] Z. Lin, T. S. Hahm, W. W. Lee, W. M. Tang, and R. B. White, Science **281**, 1835 (1998).
[38] P. H. Diamond, S.-I. Itoh, K. Itoh, and T. S. Hahm, Plasma Phys. Controlled Fusion **47**, R35 (2005).

[39]A. M. Dimits, G. Bateman, M. A. Beer, B. I. Cohen, W. Dorland, G. W. Hammett, C. Kim, J. E. Kinsey, M. Kotschenreuther, A. H. Kritz, L. L. Lao, J. Mandrekas, W. M. Nevins, S. E. Parker, A. J. Redd, D. E. Shumaker, R. Sydora, and J. Weiland, Phys. Plasmas **7**, 969 (2000).
[40]M. N. Rosenbluth and F. L. Hinton, Phys. Rev. Lett. **80**, 724 (1998).
[41]J. Candy and R. E. Waltz, J. Comput. Phys. **186**, 545 (2003).
[42]J. E. Kinsey, R. E. Waltz, and J. Candy, Phys. Plasmas **12**, 062302 (2005).
[43]F. J. Casson, A. G. Peeters, Y. Camenen, W. A. Hornsby, A. P. Snodin, D. Strintzi, and G. Szepesi, Phys. Plasmas **16**, 092303 (2009).
[44]C. M. Roach, I. G. Abel, R. J. Akers, W. Arter, M. Barnes, Y. Camenen, F. J. Casson,G. Colyer,S. C. Cowley, D. Dickinson, W. Dorland, A. R. Field, W. Guttenfelder, G. W. Hammett, R. J. Hastie, E. Highcock, N. F. Loureiro, A. G. Peeters, M. Reshko, S. Saarelma, A. A. Schekochihin, M. Valovic, and H. R. Wilson, Plasma Phys. Controlled Fusion **51**, 124020 (2009).